Infrared emitting PbS nanocrystal solids through matrix encapsulation

Journal Article

Author(s):
Moroz, Pavel; Liyanage, Geethika; Kholmicheva, Natalia N.; Yakunin, Sergii; Rijal, Upendra; Uprety, Prakash; Bastola, Ebin; Mellott, Bryan; Subedi, Kamal; Sun, Liangfeng; Kovalenko, Maksym V.; Zamkov, Mikhail
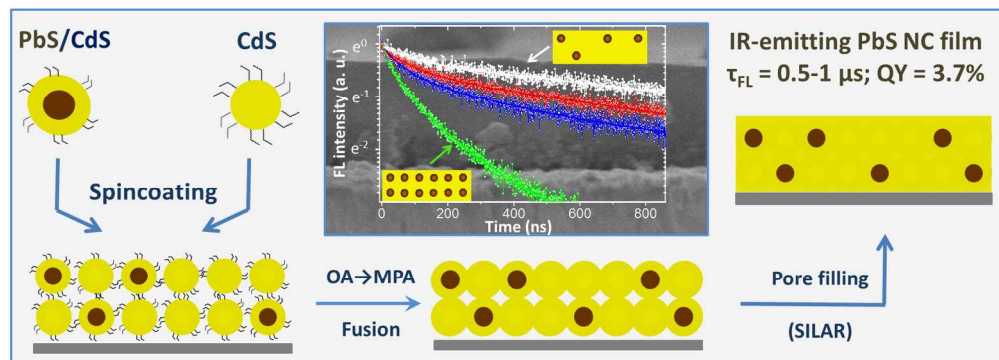
484x175mm (96 x 96 DPI)

Infrared Emitting PbS Nanocrystal Solids through Matrix Encapsulation.

Pavel Moroz[1,3†], Geethika Liyanage[3†], Natalia N. Kholmicheva[1,3], Sergii Yakunin[4,5], Upendra Rijal[3], Prakash Uprety[3], Ebin Bastola[3], Bryan Mellott[2], Kamal Subedi[3], Liangfeng Sun[1,3], Maksym V. Kovalenko[4,5], Mikhail Zamkov[1,3,].*

The Center for Photochemical Sciences[1], Department of Chemistry[2], and Department of Physics[3], Bowling Green State University, Bowling Green, Ohio 43403. Department of Chemistry and Applied Biosciences[4], ETH Zürich, Zürich, 8093, Switzerland. EMPA-Swiss Federal Laboratories for Materials Science and Technology[5], Dübendorf, 8600, Switzerland.

[†] These authors contributed equally to this work.

* zamkovm@bgsu.edu

Abstract. Colloidal semiconductor nanocrystals (NCs) are emerging as promising infrared-emitting materials, which exhibit spectrally-tunable fluorescence, and offer the ease of thin film solution processing. Presently, an important challenge facing the development of nanocrystal infrared emitters concerns the fact that both the emission quantum yield and the stability of colloidal nanoparticles become compromised when nanoparticle solutions are processed into solids. Here, we address this issue by developing an assembly technique that encapsulates infrared-emitting PbS NCs into crystalline CdS matrices, designed to preserve NC emission characteristics upon film processing. An important feature of the reported approach is the heteroepitaxial passivation of nanocrystal surfaces with a CdS

1

semiconductor, which shields nanoparticles from the external environment leading to a superior thermal and chemical stability. Here, the morphology of these matrices was designed to suppress the non-radiative carrier decay, whereby increasing the exciton lifetime up to 1 μs, and boosting the emission quantum yield to an unprecedented 3.7% for inorganically encapsulated PbS NC solids.

KEYWORDS. Lead sulfide, colloidal quantum dots, inorganic matrix, time-resolved fluorescence, quantum yield.

Near-infrared light emitting materials operating in the 700-2000 nm spectral range are commonly employed by a wide scope of applications ranging from biomedical imaging to telecommunication technologies. This spectral window is notoriously difficult to access since the emission quantum yield of most organic or inorganic infrared materials is substantially lower than that of visible-range counterparts. In light of this constraint, semiconductor nanocrystals exhibiting bright and tunable infrared fluorescence represents a promising material class for the development of near-IR technologies.[1] Of a particular interest are lead chalcogenide nanoparticles, where the quantum confinement of photoinduced charges enables an emission quantum yield (QY) of up to 50% in solution,[2-4] far above the typical QY range of indirect gap Ge or Si semiconductors.

A significant challenge for optical applications of colloidal NCs concerns their integration into transparent host matrices, which preserve their size-dependent optical properties. Besides enabling bright band gap emission, these matrices should be designed to maintain the monodispersity of embedded nanocrystals, exhibit a good thermal and chemical stability, and possess a high refractive index in order to be pertinent for utilization in waveguide-based applications. The existing matrix encapsulation strategies relying on organic polymer mixes[5-10] are reasonably successful in converting

2

nanoparticle solutions into device-compatible films, but suffer from poor thermal stability as well as polymer/semiconductor phase separation. Both of these issues can be traced back to the existence of molecular ligands preserved on surfaces of matrix-encapsulated nanocrystals. These molecules tend to desorb when thermally or electrically stimulated and are known to cause poor nanoparticle miscibility with the polymer environment. The employment of sol-gel titania matrices[11-13] has helped resolving some of these difficulties through the use of titania functional groups tethered directly to alcohol–terminated amine ligands, however, this and other emerging strategies[14-16] still suffered from poor stability of ligand-terminated NC surfaces. One viable solution to the stability problem was recently offered by the work of Kovalenko *et al.*[2] who have employed an encapsulation strategy utilizing metal chalcogenide complexes (MCC).[17,18] This methodology relied on sintering of hybrid ligands comprising MCCs into As_2S_3 amorphous matrices, which gave rise to an all-inorganic film architecture exhibiting compelling stability and a large refractive index.

Despite recent advances in enhancing the stability of nanocrystal solids,[2,19-21] the emission characteristics of these metamaterials require further improvement. In the visible range, the fluorescence quantum yield (QY) of titania-encapsulated CdSe NCs was reported to undergo a seven-fold drop upon transferring of nanoparticles into a solid form.[12] Similar trend was observed in the case of infrared emitting NCs. A spincoated film of PbSe NCs typically exhibits an emission QY of 1-2%,[22] which constitutes a significant reduction from a 50% value observed for these nanoparticles in solution.[23] The QY of PbS NC solids can be increased to 4-12% through the use of polymer matrices,[9] however, a brief exposure of these films to T = 100 C° or above results in a rapid loss of emission. Inorganic films of infrared nanocrystals are more stable but less emissive. The fluorescence QY of As_2S_3-encapsulated PbS NC solids, is around 0.1%.[24] The addition of a CdS shell prior to capping with MCC ligands results in an

3

improved QY value, however, sintering of colloidal nanocrystals into a glassy matrix[1] is still accompanied by the 4.5-time drop in the exciton lifetime.

Amongst the primary non-radiative processes that compete with the radiative decay of matrix-encapsulated NCs, two mechanisms of exciton dissociation that have been previously identified to contribute the most into quenching of the nanoparticle fluorescence.[25,26] First, dot-to-dot charge transfer can lead to the formation of a "dark" excited state, whereby reducing the probability of the radiative recombination. Likewise, an interparticle energy transfer increases the probability of defect filling due to multiple dot-to-dot transitions, thus contributing to a non-radiative decay. Second, charge trapping on dangling bonds and nanocrystal/matrix interfaces can cause exciton dissociation followed by a non-radiative relaxation of carriers. With respect to the interparticle charge transfer process, the rate of dot-to-dot carrier tunneling was previously shown to have a nearly exponential dependence on the width and the height ($\sqrt{\Delta E}$) of the potential barrier separating adjacent nanocrystals.[27] Therefore, the charge transfer pathway of exciton dissociation can be readily suppressed by choosing a wide gap matrix material or by employing a sufficient interparticle separation.

Trapping of excited carriers on surfaces and interfaces of encapsulated nanoparticles, however, represents a more serious problem. In the case of polymer or titania matrices, the surfaces of encapsulated nanocrystals retain original, long-chain organic ligands to help lower the density of surface traps.[12] This strategy, however, suffers from the propensity of ligand molecules to detach from NCs as a result of a thermal or electrical stimulation. The desorption of ligands inevitably compromises the stability of the NC emission in a film, regardless of the stability of the matrix medium. In the case of glassy matrices, hybrid or fully inorganic ligands serve as a surface passivation layer,[1,28-33] which warrants a compelling thermal stability. The glass sintering step, however, may result in an imperfect surface passivation,[34] which could be partly responsible for a low emission yield observed in the case of As_2S_3-encapsulated PbS NC solids. Ideally, well defined stoichiometric relationships should exist

4

between encapsulated nanoparticles and a matrix medium, which itself should exhibit a high thermal and chemical stability.

Here, we demonstrate a solution-phase assembly of PbS nanocrystals into inorganic solids exhibiting bright infrared emission and superior thermal stability. The reported methodology takes the advantage of crystalline semiconductor matrices, heteroepitaxially bonded to surfaces of encapsulated PbS nanocrystals. Such passivation strategy promotes a reduced density of surface traps, which is manifested in this work through the observation of a compelling emission quantum yield. The suppressed defect trapping is also apparent through the detection of long exciton lifetimes approaching 1 microsecond for best-performing films. This constitutes a noticeable improvement over NC solids assembled *via* conventional ligand-linking or amorphous-matrix strategies.

Results and Discussion.

The matrix encapsulation technique developed in this work builds upon a recently reported semiconductor matrix embedded nanocrystal array (SMENA) approach, [35,44] which allows for a gap-free inclusion of colloidal NCs into host matrices of wide band gap semiconductors. Typically, nanocrystals are encapsulated using a three-step procedure (see Fig. 1a). First, hot-injection chemistry is used to grow monodisperse PbS NCs, onto which a shell of a lattice-matched semiconductor (CdS) is deposited. The matrix semiconductor is chosen to form a type I band edge alignment with PbS, thus promoting core-localization of both carrier types (Fig. 2a). In the second step, core/shell NCs (PbS/CdS) are spincoated onto a suitable substrate, capped with thermally degradable ligands, and subsequently heated to 140-160 °C to promote the ligand removal (as monitored by FTIR) and to induce merging of respective shells (CdS-CdS) *via* the crystallographic fusion process. In the final step, the pores of the CdS matrix are filled with an additional CdS material through the successive ionic layer adsorption and reaction (SILAR) method.[36] This step helps passivating exposed surfaces of the CdS matrix (thus neutralizing carrier traps) and increases an average refractive index (n) of the film. The pore filling step also promotes an enhanced stability of the PbS NC array.
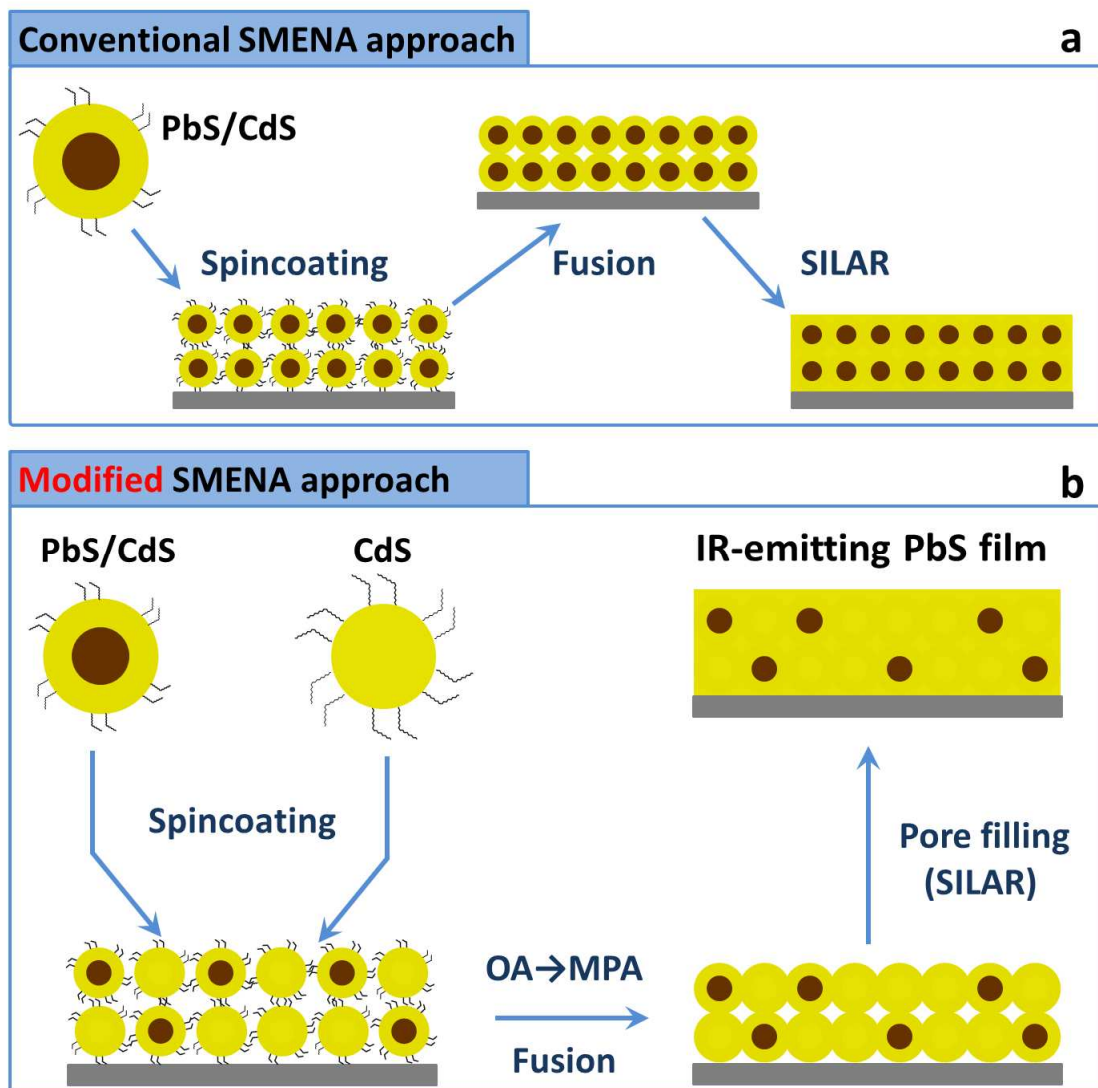
5

Figure 1. (a). Illustration of the key steps involved in the development of conventional Semiconductor Matrix-Encapsulated Nanocrystal Arrays (SMENA). These stages include colloidal synthesis of PbS/CdS core/shell NCs (step 1), spincoating or dip-coating of NC films (step 2), exchange of bulky ligands with thermally degradable MPA molecules, crystallographic fusion of core/shell NCs performed using a layer-by-layer deposition (steps 3), and in-filling the pores of the resulting matrix

6

with additional CdS (step 4). (b). In a modified SMENA approach, PbS/CdS NCs are mixed with CdS-only NCs (of a similar diameter) in the first step.

To enhance the radiative portion of the excited state decay in matrix-encapsulated nanocrystals, the localization of photoinduced charges should be increased. In a conventional SMENA approach,[34] this goal is achieved by augmenting the thickness of the shell, ΔH, in core/shell precursor NCs, which determines the ultimate value of the minimal edge-to-edge distance between PbS domains in the film (R_{edge} = 2 x ΔH). Indeed, larger R_{edge} results in the suppression of the interparticle charge and energy transfer processes, leading to enhanced probability of the radiative recombination. This situation is illustrated in Fig. 2b, showing the relationship between the interparticle charge transfer rate and the R_{edge} distance in the film. It is assumed that the charge tunneling rate has a single exponential dependence on the width of the potential barrier separating neighboring nanocrystals. According to Wentzel–Kramers–Brillouin (WKB) approximation, this rate is proportional to $\Gamma \sim \exp(-2(2m\Delta E/\hbar^2)R_{edge})$, where ΔE is the height of the potential barrier between electron or hole states in adjacent NCs. The regime of strong charge localization is achieved when the coupling energy $\beta = \hbar\omega\Gamma$ drops below kT, known as Mott insulator regime. Since the carrier localization is more pronounced in dots with a larger core size (Fig. 2a), the characteristic R_{edge} distance at which such transition occurs diminishes with the growing diameter of the PbS domain. This trend is clearly seen in Fig. 2b through the comparison of the inter-dot coupling energy for the cases of 4-nm and 6-nm diameter PbS NCs embedded into CdS matrices. For example, the value of R_{edge} associated with the insulator transition in 4-nm-PbS/CdS solids is about 2 times greater than that of 6-nm-PbS/CdS. We note that while x-axis in Fig. 2b is given only in relative units of scale, it preserves the correct lengths ratio corresponding to insulator transitions between different dot diameters.
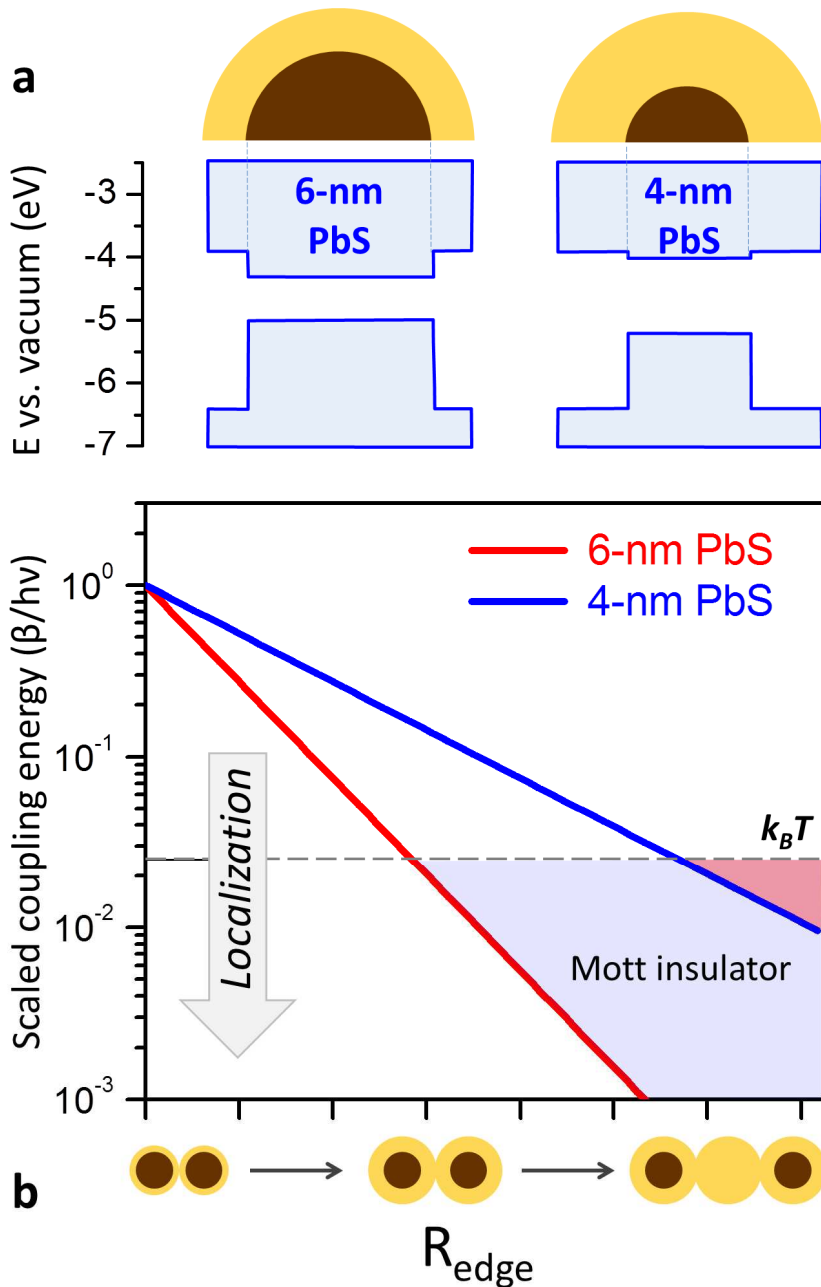
Figure 2. (a). Energy diagram showing a relative alignment of conduction and valence band edges in 4.0-nm PbS/CdS and 6.0-nm PbS/CdS core/shell nanocrystals. (b). WKB tunneling approximation of the coupling energy dependence on the interparticle distance (R_{edge}) for the two material systems shown in (a). The colored areas indicate the regime of strongly localized charges.

8

According to Fig. 2b, achieving a strong localization of photoinduced charges in small-diameter PbS NCs requires growing a thick CdS shell needed to compensate for a shallow potential barrier to electrons in PbS (see Fig. 2a). A possible drawback of this strategy is the propensity of thicker shells to cause an excessive interfacial strain, which typically relaxes through the formation of defects, whereby introducing additional non-radiative decay channels.[37-39] Alternatively, the width of the potential barrier separating adjacent PbS NCs could be increased by replacing a portion of PbS NCs with CdS dots of the same diameter, as illustrated in Fig. 1b. Such strategy would result in a sufficient interparticle separation needed for a strong carrier localization without the need for an additional shell growth. Within this approach, the balance between the filling factor (ff) and the emission quantum yield of embedded PbS NCs can be controlled by varying the ratio of PbS/CdS to CdS nanoparticle precursors in the mixture. For instance, increasing the volume fraction of PbS NCs embedded into CdS matrices leads to the reduction of an average R_{edge} distance between neighboring PbS domains. This results in the enhancement of the filling factor and a concurrent drop in fluorescence (FL) quantum yield due to an incomplete localization of excited carriers in electrically coupled PbS cores. Conversely, a low volume fraction of PbS NCs should promote a greater emission QY due to an enhanced carrier localization but would lead to a relatively low filling factor.

To explore the effect of the interparticle separation, R_{edge}, on the PbS exciton decay, we have fabricated two sets of nanoparticle solids representing two different strategies for tuning the value of R_{edge}. In the first approach, the R_{edge} distance was controlled through a conventional SMENA technique, by adjusting the thickness of the CdS shell in PbS/CdS core/shell nanocrystal precursors. For the second set of films, we have used a modified-SMENA strategy wherein the value of R_{edge} was adjusted by introducing a tunable fraction of CdS nanoparticles. Core/shell PbS/CdS NCs used in both sets of experiments were fabricated using a cation exchange approach.[2] This method benefits from a precise control of the shell thickness, a parameter, which determines the ultimate value of R_{edge} in both film

9

architectures. A characteristic TEM image of core/shell PbS/CdS NCs featuring a 2.7-nm PbS core capped with a 1.3-nm CdS shell is shown in Fig. 3a and 3b. A uniform placement of the CdS shell around the PbS core is evident in high resolution TEM images of PbS/CdS NCs (Fig. 3b and Fig. SF6).
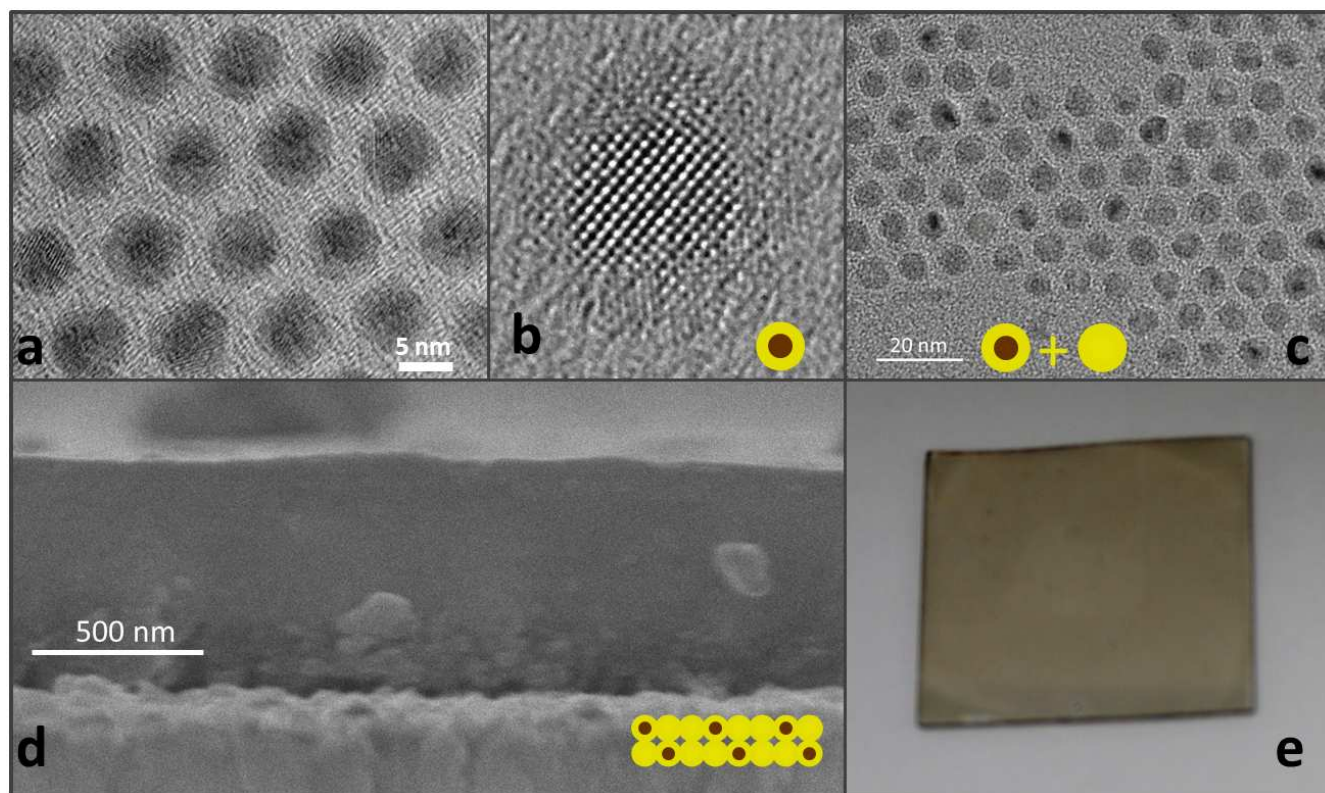
Figure 3. (a,b). High resolution TEM images of 2.7-nm PbS nanocrystals coated with a 1.3-nm CdS shell. (c). The mixture of PbS/CdS NCs and 5.0-nm CdS NCs prior to the deposition on a glass substrate. Scanning electron microscope (d) and photo (e) images of a CdS-encapsulated PbS NC film.

The fluorescence (FL) lifetime of PbS nanocrystal solids assembled using a conventional SMENA strategy (Fig. 4a) increases with the growing interparticle separation in the film, which is consistent with a diminishing probability of exciton dissociation through charge and energy transfer processes. It was previously shown that the characteristic timescale for such interparticle transfer is given by the fast component of the FL intensity decay, as illustrated in Fig SF1, while the slow component represents charge trapping on surfaces of unpassivated CdS matrices.[40] The fast exponent of the film emission is therefore limited to charge and energy transfer processes that result in non-emissive states. Notably, the

10

two transfer mechanisms have distinctly different R_{edge} dependences. According to WKB approximation, the rate of charge tunneling between resonant states decays exponentially with R_{edge}, while the rate of energy transfer diminishes as R^6_{edge} in accordance with the nonradiative dipole–dipole coupling approximation (Förster resonance energy transfer).[41] The comparison of experimentally measured τ^{FL}_{fast} with the WKB ($\sim e^{\alpha R_{Edge}}$) and FRET ($\sim r^6$) model curves in Fig. 4b reveals that charge transfer is a more likely mechanism to contribute into exciton dissociation. Indeed, the observed transfer times exhibit a nearly single-exponential dependence on R_{edge}, which is characteristic of a charge tunneling process, and not the energy transfer, which is strongly affected by small changes in R_{edge}. This suggests that the charge transfer between adjacent dots in the matrix is the primary mechanism responsible for the formation of non-emissive states.
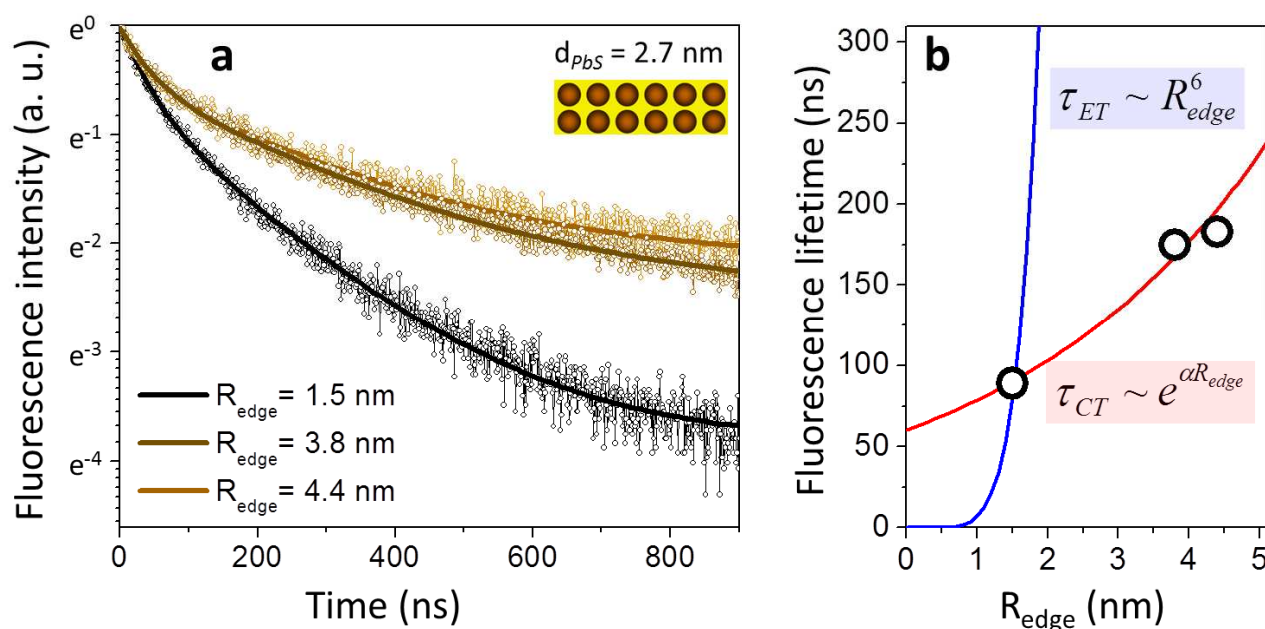

Figure 4. (a). Fluorescence intensity decay of conventional SMENA films representing different R_{edge} values. (b). Measured exciton lifetimes for CdS-encapsulated PbS NCs and their fitting by a model according to WKB (charge transfer) and dipole–dipole coupling (energy transfer) approximations.

In the case of a conventional SMENA approach, the fluorescence lifetime of matrix-encapsulated nanocrystals did not exceed $\tau = 190$ ns, which is far below the 2.8 microsecond lifetime observed for the

11

same nanocrystals in solution (see Fig. SF2). Even with further increases in the shell thickness beyond 3-4 monolayers, the emission lifetime remained roughly the same. Taking into account a significant suppression of the interparticle charge transfer for such large values of R_{edge}, the short lifetime has been tentatively attributed to a continuous build-up of the interfacial strain, manifested by the growing ratio of the trap state to band gap emission (see Fig. SF3).[33] Decay of trapped carriers creates a broad band emission, which overlaps with the PbS FL peak. Subsequently, despite an enhanced exciton localization in solids featuring large interparticle distances, strong emission within a narrow spectral band cannot be reached through a conventional SMENA architecture. On the contrary, the modified SMENA approach allows enhancing the interparticle separation without the need for an epitaxial growth of large shells. By including CdS nanoparticles within PbS/CdS matrices, we aim to facilitate the suppression of charge and energy transfer between adjacent PbS nanoparticles, while preventing the formation of rate-limiting defects.

To explore optical properties of modified-SMENA solids comprising a mixture of CdS and PbS/CdS NC precursors, we have fabricated several films featuring an increasing fraction of CdS to PbS nanoparticles. The volume fraction of PbS NCs in these solids was calculated based on the known ratio of PbS to CdS particle absorbance. Namely, when CdS and PbS/CdS core/shell colloids are fused into a film, the average interparticle distance, R_{edge}, becomes greater than twice the thickness of the CdS shell as the distance between the PbS dots is now enhanced by the presence of interstitial CdS domains. To determine the relationship between molar concentrations of both nanoparticle types and the partial number density of these nanocrystals in a mixture, precursor solutions of mixed nanoparticles were deposited onto a TEM grid and analyzed. According to Fig. 5e, the ratio of each nanoparticle type (PbS/CdS core/shell versus CdS dot) can be easily obtained by identifying the corresponding populations of each dot in the TEM specimen. The core/shell nanocrystals can be differentiated by their larger radii and darker shading, as indicated by arrows in a characteristic TEM image (Fig. 5e), featuring 4.3-nm CdS and 5.2-nm PbS/CdS NCs. Since the initial concentrations of each colloid prior to TEM sampling were known, the number density of each nanocrystal type in a film can be estimated. The ratio

of CdS to PbS/CdS dots in the film is then used to estimate the PbS volume fraction, v_{PbS}, according to the following equation (see Supporting Information for details of calculation):

$$v_{PbS} = \frac{(n+1)^2 \times \frac{4}{3}\pi R_{core}^3}{(nD_C + D_{P/C})^3} \qquad (1)$$

where $n = N_{PbS}/N_{CdS}$, and R_{core} is the average radius of the PbS core domain in PbS/CdS core/shell NCs.
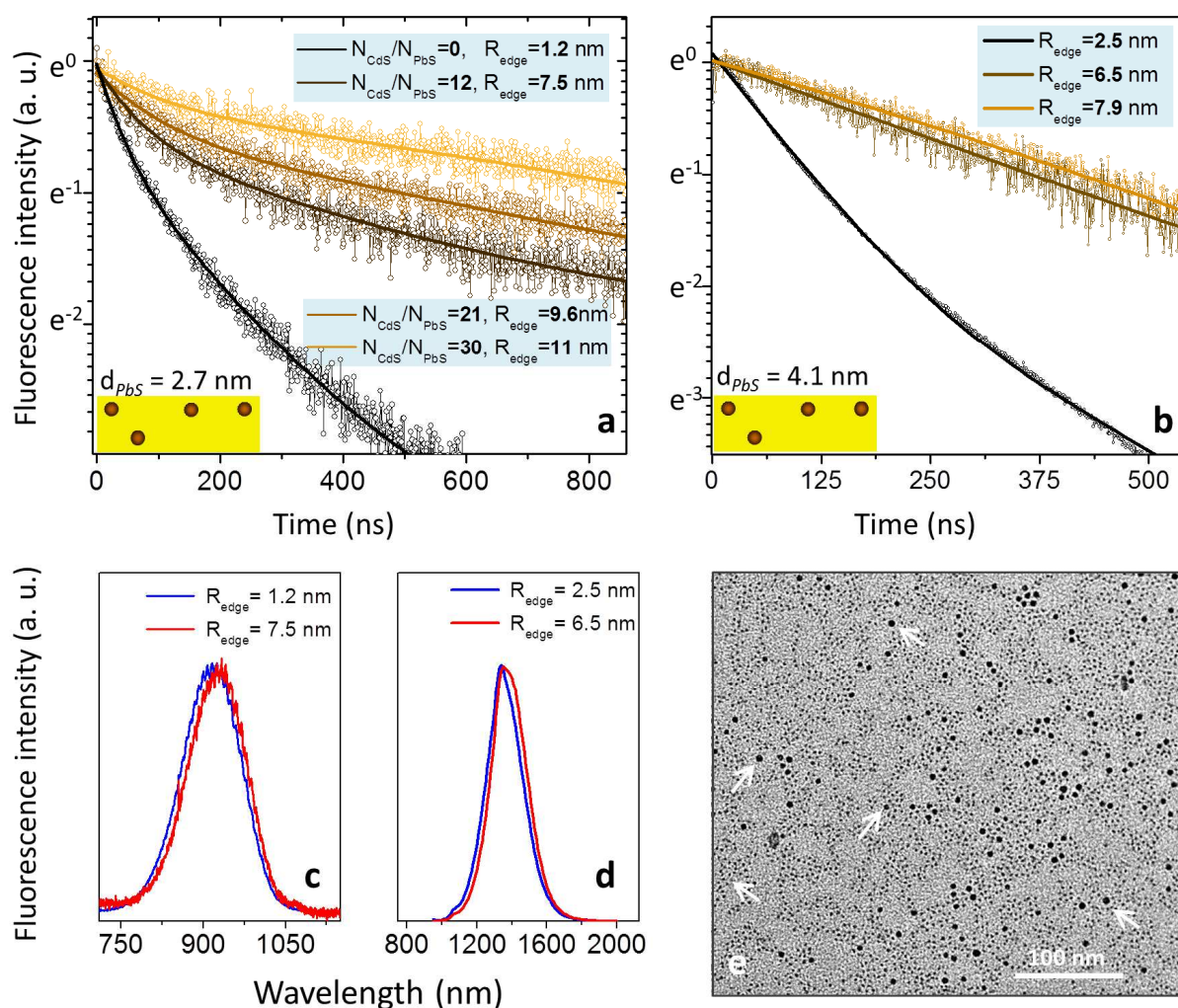

Figure 5. Fluorescence intensity decay of near-IR emitting PbS NCs (a) d=2.7 nm and (b) d=4.1 nm encapsulated into CdS matrices as a function of increasing N_{CdS}/N_{PbS} "precursor nanoparticle" fraction. (c). Steady-state emission of modified-SMENA films (d_{PbS} = 2.7 nm) featuring N_{CdS}/N_{PbS}=0 (blue curve) and N_{CdS}/N_{PbS}=12 (red curve). (d). Steady-state emission of modified-SMENA films (d_{PbS} =

13

4.1 nm) representing $N_{CdS}/N_{PbS}=0$ (blue curve) and $N_{CdS}/N_{PbS}=4$ (red curve). (e). A characteristic TEM image of 4.3-nm CdS and 6.0-nm PbS/CdS NC mixture. Arrows mark the location of PbS/CdS core/shell structures.

Figure 5a shows the FL intensity decay of mixed CdS (d_{CdS} = 4.3 nm) and CdS/PbS (d_{PbS} = 2.7 nm) NC solids fabricated using a modified SMENA approach. As expected from WKB approximation, the FL lifetime increases with growing R_{edge}, reflecting a simultaneous decrease in the cumulative rate of interparticle transfer processes. The fastest decay in Fig. 5a (R_{edge} = 1.2 nm) corresponds to a solid containing no CdS NCs (conventional SMENA). A relatively thin CdS shell ($\Delta H \approx 1$ nm) used in this case enabled only a partial localization of charges, leading to a charge transfer-limited lifetime of about 95 ns. The addition of CdS NCs to PbS/CdS precursor nanoparticles increases the interparticle separation from 1.2 to 11 nm (Fig. 5a), bringing the maximum R_{edge} to more than twice the value accessible through a conventional SMENA approach. The enhanced interparticle separation results in a stronger localization of photoinduced charges (as illustrated in Fig. 2b), which causes the FL lifetime to increase (Fig 5a). A particularly interesting trend was observed for large values of R_{edge}. For these matrices, the lifetime of PbS excitons climbed to an unprecedented 0.98 μs (determined by a 1/e intensity drop), which constitutes a four-fold increase over best-performing NC emitters fabricated through a conventional SMENA approach. We note that the exciton lifetime for these nanocrystals in solution is 2.8μs (Fig. SF2), which implies that a substantial fraction of excitations recombine radiatively, setting the upper limit of the FL QY to nearly $100*\tau_{FL}/\tau_{radiative}$ = 10% (although absolute QY was not measured for these samples). Likewise, the observed exciton lifetime was found to be enhanced relative to those of previously reported PbS NC film architectures utilizing hybrid molecular ligands.[2] This phenomenon can be tentatively attributed to a suppressed non-radiative decay in matrix-passivated nanocrystals. The saturation of the fluorescence lifetime in modified-SMENA films emitting at $\lambda \approx 1300$ nm occurs faster than in small-diameter PbS NC films (see Fig. 5b), with the longest lifetime

14

of τ = 480 ns. An enhanced lifetime of band gap excitons in mixed PbS NC films is consistent with the reduced volume fraction of PbS NCs in comparison with conventional SMENA solids. Finally, according to Figs. 5c,d, the increase in R_{edge} value gives rise to a < 20 nm redshift of the emission peak, as expected due to the delocalization of the electronic wave functions into the CdS matrix.

An absolute value of the emission quantum yield was determined for films comprising large-diameter PbS NCs (λ_{FL} ≈ 1300 nm). We note that these films did not yield the best exciton lifetime, however, were more compatible with the experimental setup in use. The detection methodology was adapted from the one described in Ref. 45, and was designed to eliminate the use of a reference dye and to provide the possibility for simultaneous measurement at excitation wavelength of absorbance, which is corrected to reflectance and scattering losses at integrating sphere. According to these measurements (summarized in Table ST1), the highest value of the emission quantum yield of QY=3.7% was realized for solids featuring R_{edge} of 7.9 nm. To the best of our knowledge, this value represents the highest reported emission QY for inorganic nanocrystal films emitting in the infrared range. The difference between the observed QY value in a solid and a typical QY range for these nanoparticles in solution (10-30%) is attributed to the onset on non-radiative decay pathways (trapping and charge transfer) upon the transfer of colloidal nanoparticles onto a substrate.

Another relevant property of modified SMENA films that merits discussion is the linewidth of the emission peak. Application of luminescent films in light-emitting technologies often benefits from a spectrally narrow emission profile. Our estimates show that the peak width of modified-SMENA films (FHWM = 165 nm, @ λ = 970 nm) increases compared to that of OA-capped PbS NC in solution (FHWM = 120 nm, @ λ = 950 nm). However, the fusion of core/shell NCs into a solid doesn't not seem to contribute much to broadening of the emission profile, as OA-capped PbS/CdS NCs in solution exhibit FHWM of 160 nm. Indeed, the primary enhancement of the peak width occurs as a result of the shell growth, an important step, which also results in the improvement of the FL QY.
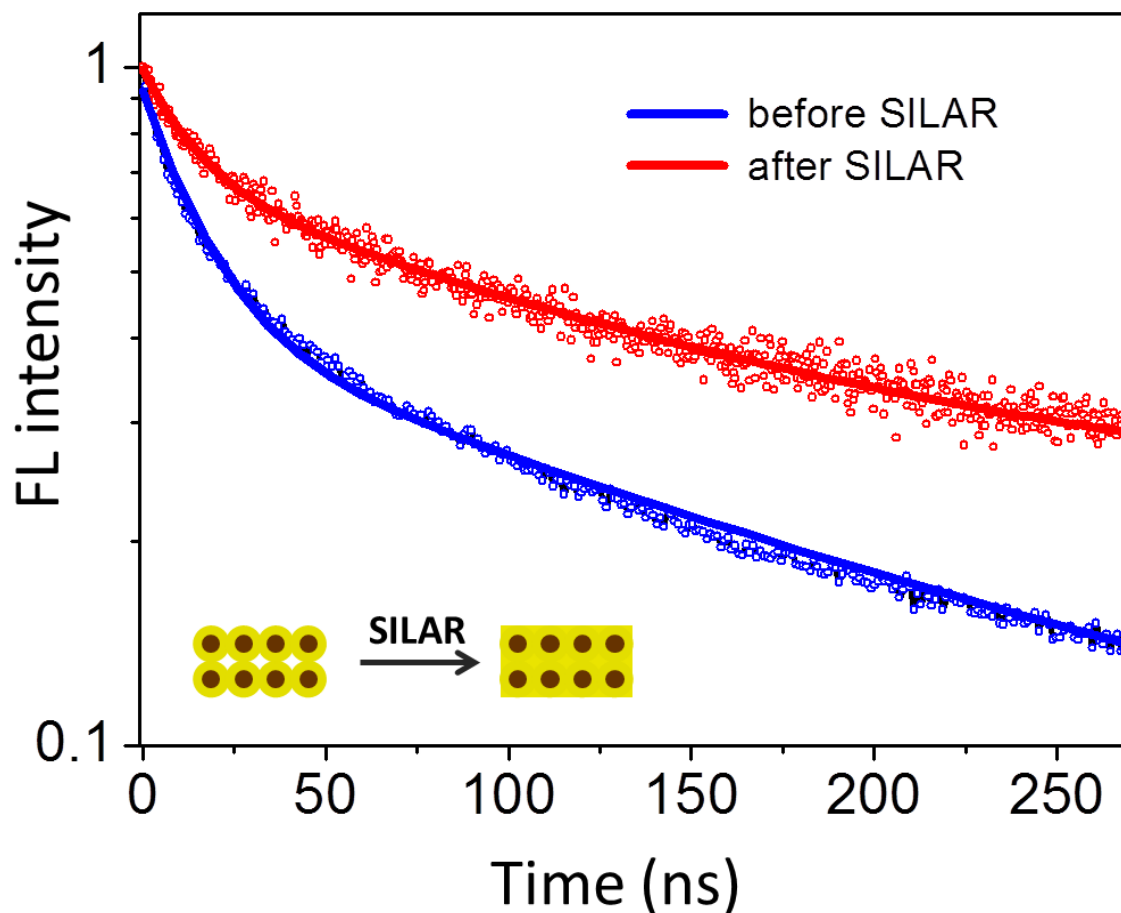
15

Figure 6. Suppression of charge trapping on the surface of PbS/CdS SMENA films (R_{edge}= 1.5 nm,

d_{PbS} = 2.7 nm) by additional SILAR passivation. The red curve represents an increased exciton lifetime

following the SILAR treatment.

In order to reduce the density of dangling bonds in nanocrystal matrices, interparticle gaps between

fused core/shell structures were partly filled with additional CdS. To this end, several SILAR cycles

were applied resulting in a deposition of 3-4 CdS monolayers. Previous works have shown[34] that such

treatment increases the refractive index of the nanocrystal film through partial filling of void areas.

According to Fig. 6, application of 6 SILAR cycles to a CdS-encapsulated PbS NC film featuring R_{edge}

of 1.5 nm results in a 55% increase in the FL lifetime. In particular, the slower component of the FL

16

intensity decay, which is associated with charge tapping has increased from $\tau_{FL,\,slow} = 90$ to $\tau_{FL,\,slow} = 150$

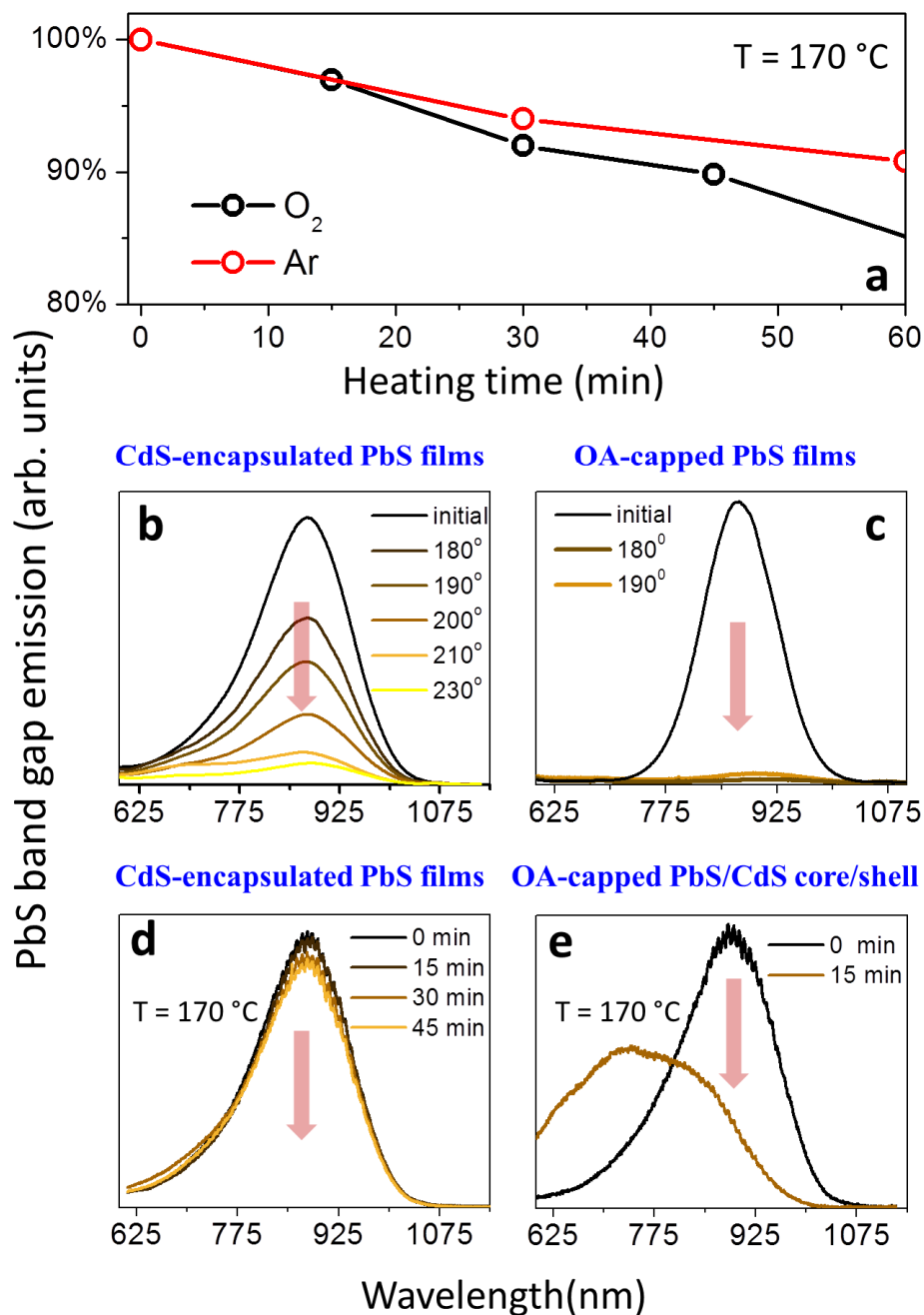ns, reflecting the reduction in the rate of carrier trapping.

Figure 7. (a). Temporal evoluition of the band-edge emission peak area for CdS-encapsulated PbS

NC arrays ($R_{egde} \approx 2.8$ nm) fabricated using a modified-SMENA approach. (b,c). Comparison of the

17

thermal stability of OA-capped (c) and CdS-encapsulated (b) PbS NC arrays, fabricated using a modified-SMENA approach. (d,e). Temporal evolution of the emission peak for films expoosed to T=170 °C in air. The comparison is drawn between CdS-encapsulated PbS NC arrays (d) and OA-capped PbS/CdS core/shell NCs on a substrate (e).

Improving the thermal stability of NC solids is important for their deployment in light-emitting devices, as many of those applications are subject to the generation of heat. In the present approach, the presence of heteroepitaxial bonding between NC surfaces and the matrix semiconductor is expected to prevent low-temperature oxidation, deferring the thermal degradation of NCs to occur only at higher temperatures *via* the phase transition of the lattice. Here, we test this hypothesis by comparing thermal stability of modified-SMENA films (R_{edge} = 2.8 nm, SILAR treated) with that of oleic acid (OA)-capped PbS NC films. To this end, the intensity of band edge emission in both solids was plotted versus the substrate temperature. According to Figs. 7b,c, heating of matrix-encapsulated (b) and OA-passivated (c) PbS NCs in air results in a gradual drop of the emission intensity, which was taken as a sintering temperature of PbS. In the case of CdS-encapsulated PbS NCs, sintering occurred at T ≈ 200 °C, which is 90-100 °C above that of OA-capped PbS NC solids. Interestingly, the thermal stability of modified-SMENA PbS solids does not arise merely from the presence of the CdS shell on PbS surfaces. According to Figs. 7d,e, oleic acid-capped PbS/CdS NCs (ΔH_{CdS} = 1.2 nm) placed on a hot substrate undergo a much faster degradation of the band gap emission then modified SMENA films fabricated from the same core/shell nanoparticles. This result strongly suggests that the crystallographic fusion of core/shell precursors into a solid is essential for enhancing the stability of encapsulated PbS NCs. In the final stability test, we have looked into the temporal degradation of the film versus time by recording the

18

changes in the emission intensity after the heat was applied to the substrate. The two curves in Fig. 7a,

illustrate the reduction in the emission intensity of matrix-encapsulated PbS NCs for films kept in argon

(red) and air (blue). A slightly faster decay of the latter curve suggests that oxidation is partly

responsible for the loss of emission at elevated temperatures. These experiments demonstrate an

enhanced heat resistance of matrix-encapsulated PbS SMENA solids as compared to organic-interlinked

nanoparticle films.

Conclusions.

In conclusion, a novel strategy for processing of PbS nanocrystal solids exhibiting bright infrared

emission is demonstrated. The reported methodology benefits from the use of inorganic CdS host

matrices to provide a stable passivation of nanoparticle surfaces while preserving some degree of

quantum confinement. The morphology of encapsulating matrices was judiciously optimized to induce

the suppression of non-radiative decay processes associated with surface carrier trapping and

interparticle charge transfer. This allowed extending exciton lifetimes up to 1 microsecond, which

constitutes at least a two-fold enhancement over ligand-based passivation strategy. The suppressed

carrier trapping has given rise to a high emission quantum yield of $QY_{solid} = 3.7\%$ in the infrared range,

while inorganic matrix medium warranted a superior thermal and chemical stability of fabricated

nanocrystal solids.

Experimental Section.

Materials. 1-octadecene (ODE, 90% Aldrich), oleic acid (OA, 90% Aldrich), lead(II) oxide powder

(PbO, 99.999% Aldrich), cadmium oxide (CdO, 99.99%, Aldrich), sodium sulfide nonanhydrate

(Na$_2$S·9H$_2$O, 98% Alfa Aesar), sulfur (S, 99.999% Acros), ethanol (anhydrous, 95% Aldrich), methanol

(anhydrous, 99.8% Aldrich), toluene (anhydrous, 99.8% Aldrich), isopropanol (anhydrous, 99.8%

Acros), octane (anhydrous, 99% Aldrich), hexane (anhydrous, 95% Aldrich), 3-mercaptopropionic acid

19

(3-MPA, 99% Alfa Aesar), bis(trimethylsilyl) sulfide (TMS$_2$, Aldrich, synthetic grade), chloroform (anhydrous, 99%, Aldrich), cadmium acetate dihydrate ((CH$_3$COO)$_2$Cd·2H$_2$O, 98%, Acros), zinc acetate (98+% Acros), acetone (anhydrous, Amresco, ACS grade) were used as received without any further purification. All reactions were performed under argon atmosphere using the standard Schlenk technique. Glass substrates (Corning Microscope Slides, 0.96-1.06 mm, 0215 Glass) were obtained from Corning Inc.

Methods.

Fabrication of PbS nanocrystals. PbS NCs were fabricated according to a procedure adapted from Hines *et al.*[42] In a typical synthesis, a mixture of 0.49 g (2mmol) PbO in 18 mL of ODE and 1-16 mL of OA (increasing the amount of OA results in larger NCs) was degassed in a three-neck flask at 120°C for 2 hours, switched to Argon, and heated to 135 °C. Meanwhile, 10 mL of ODE was degassed for two hours at 120°C and allowed to cool down to room temperature. Then, 0.21 ml of (TMS)$_2$S was added carefully into the flask and the resulting (TMS)$_2$S/ODE mixture was injected into the Pb precursor solution at 135°C, while stirring. The reaction was stopped after 0-5 minutes (longer reaction time leads to larger NCs) by removing the flask from the heating mantle and placing it into an ice water bath. The nanocrystals were isolated from the mixture by precipitating with acetone, centrifuging, and re-dispersing in toluene. The cleaning procedure was repeated 2-3 times, after which nanocrystals were re-dispersed in a minimal amount of hexane (4-5 ml).

For example, to fabricate PbS NCs with an exciton absorption feature centered at 1050 nm (d$_{PbS}$ = 3.5 nm), 2 mL of OA was used and the growth time was limited to 1 min. For NCs with a 1S peak at 1300 nm (d$_{PbS}$ = 4.6 nm), 14 mL of OA was used with the growth time of 4 min. For NCs with a 1S peak at 930 nm (d$_{PbS}$= 3.0 nm), 1.5 mL OA was used with the reaction time of 1 min.

Synthesis of PbS/CdS core/shell NCs. The growth of the CdS shell on PbS NCs was performed using a cation exchange methodology.[2] To this end, 0.95 g (7.6 mmol) of CdO was dissolved in 10 ml of OA and 18 ml of ODE under Ar at 235 °C until the solution became clear. Then, the temperature of this solution was set at 130°C. Meanwhile, 4 ml of PbS seed nanocrystals (d = 4.2 nm) solution in hexane (concentration 10 mg/ml) was kept under argon gas flow at 80°C for 2 minutes to remove excess of solvent and then was injected into the cadmium solution under vigorous stirring. The reaction mixture was kept at 135 °C for 7 minute and then stopped by immersing the flask in the ice water bath. The purification process included the separation of nanoparticles from the solution with ~30 ml of ethanol,

centrifugation and dissolution of the precipitated nanocrystals in a minimal amount of hexane. The cleaning cycle was repeated two times. Under these conditions the absorbance peak was found to blue-shift by 330 nm (approx. 0.8 nm of the CdS shell). The growth of the CdS shell depended on the size PbS NCs and the reaction time. Longer reaction times, higher temperatures and higher ratios of OA/ODE were used to obtain a thicker shell of CdS.

To determine the shell thickness in thin-shell nanocrystals (where TEM images do not provide the sufficient accuracy) the following approach was used. First, the size of original PbS dots was determined from the position of the exciton absorption edge. The reduction in the average size of the PbS domain upon Pb^{2+} to Cd^{2+} cation exchange was determined from the new position of the PbS exciton peak. The thickness of the shell was then calculated under the assumption that the diameter of the PbS/CdS core/shell structure remained the same as the diameter of the original PbS dot.

Synthesis of CdS nanoparticles. For the fabrication of CdS seeds an approach proposed by Yu *et al.* was used.[43] The mixture of 0.0384 g (0.3 mmol) CdO, 1 ml OA and 11 ml ODE in a 50 ml 3-neck flask was heated to 300ºC until solution turned optically clear and colorless. Then, the temperature of the reaction mixture was set up at 250ºC and a sulfur precursor solution made by dissolving sulfur powder 0.0048 g (0.15 mmol) at 200ºC in ODE (4.5 mL) was quickly injected. The reaction was stopped by removing the flask from the heating mantle after 5-9 minutes. CdS NCs were separated from the solution by precipitation with methanol followed by repeated hexane/methanol extractions. The final nanocrystals had diameter 3.5-4.5 nm (depending on the reaction time) and were stored in hexane.

Preparation of the glass substrate. Before the deposition of nanocrystals the glass substrates were cleaned and dry for better performance. To this end, glass squares 2.5 cm x 2.5 cm were washed with detergent (Alconox) and rinsed in deionized water. Subsequently, substrates were sonicated in methanol, acetone and isopropanol for 5 minutes in each solvent and dry under argon flow.

Fabrication of nanocrystal solids. The fabrication of all-inorganic NC films was performed using previously reported Semiconductor Matrix Encapsulated Nanocrystal Array (SMENA) methodology.[44]

To deposit a layer of all-inorganic CdS-encapsulated NC film onto the FTO/glass substrate, 3-5 drops of the PbS/CdS core/shell NC solution in hexane (concentration 10mg/ml) were placed onto the spinning at 3000 rpm glass until the surface was covered and then dry. To replace original OA ligands with thermally-degradable MPA molecules, 7-10 drops of MPA/Methanol solution (ratio1:4) were deposited on the center of the glass slide, soaked for 10 seconds and spun at 3000 rpm for 10 seconds.

21

After the MPA treatment, the film was washed by covering with 10 drops of methanol and spinning the slide for 10 seconds, followed by rinsing with octane in the same manner. Upon the deposition of 2 layers the films were annealed at 120-140°C for 15 mins. The total of 4-6 layers were deposited. To fabricate modified SMENA with additional CdS NCs, the initial solution of PbS/CdS NCs was mixed with the CdS solution in ratios, which were calculated by dividing the optical densities at the 1st excitonic peak for CdS ($\lambda = 430$ nm) and PbS/CdS NCs ($\lambda \approx 850\text{-}900$ nm) colloidal precursors. The final volume ratios of nanocrystals were calculated using TEM data from utilized solutions, as discussed in the text.

In-filling of SMENA pores with CdS. For the pore-filling process, the successive ionic layer adsorption and reaction (SILAR) method was applied.[36] Briefly, the deposition of additional layers of CdS was conducted by sequential soaking of the annealed NC films in methanol solutions of Cd and S precursors. For this purpose, the cadmium bath was prepared by dissolution of 0.113 g of cadmium acetate in 20 mL of methanol and the sulfur bath by placing 0.098 g of $Na_2S \cdot 9H_2O$ in 20 mL of methanol. One SILAR cycle included soaking of the film in the cadmium bath for 1 minute, then rinsing the film with methanol for 1 minute, then soaking it in the sulfur bath for 1 minute with sequential washing in methanol. 2-10 cycles of pores filling process was applied for all-inorganic films followed by annealing at 150 °C for 15 minutes.

Characterization. Absorbance spectra were recorded using CARY 5000 and Shimadzu UV-3600 UV-vis-NIR spectrophotometers. Photoluminescence spectra were recorded using a Jobin Yvon Fluorolog FL3-11 fluorescence spectrophotometer and using a home-built photoluminescence spectroscopy apparatus including an Argon ion laser Reliant 150M (Laser Physics), an Acton SP-2357 Monochromator (Princeton Instrument) and an IR detector PDA30G (Thorlabs). High-resolution transmission electron microscopy (HR-TEM) measurements were carried out using JEOL 3011UHR and 2010 transmission electron microscopes, operated at 300 and 200 kV, respectively. To prepare a TEM sample, a small amount of NC film was scraped, dispersed in toluene by sonication, dropped onto a carbon-coated copper grid, and allowed to dry in air. FL lifetime measurements in 900nm region were performed using a time-correlated single photon counting setup utilizing SPC-630 single-photon counting PCI card (Becker & Hickle GmbH), picosecond diode laser operating at 400 nm, as an excitation source (Picoquant), an id50 avalanche photodiode (Quantique), and long-pass optical filters with edges at 400nm, 532nm, 750nm and 900nm. Time – resolved PL traces in 1300 nm region were

22

obtained by Time-Correlated Single Photon Counting (TCSPC) system based on InGaAs TE cooled single photon avalanche photodiode(ID Quantique) of 200 ps time resolution, adjusted for 10% quantum efficiency, SPC-130-EM Counting Module and BDL-488-SMN laser (Becker & Hickle) with pulse duration of 50 ps and wavelength of 488 nm, CW power equivalent of about 0.5 mW, externally triggered at 1MHz repetition rate. PL emission from the samples passed through long-pass optical filters with edges at 500nm 1300 nm in order to reject excitation laser line and possible emission from CdS matrix.

Fluorescence quantum yield measurements. The absolute value of quantum yield was measured by method, similar to the one described in Ref. 45. In our case the advantage was the elimination of a reference and a possibility of simultaneous measurement of absorbance at excitation wavelength, with correction to reflectance and scattering losses using integrating sphere. As excitation source CW Laser Diode Module with wavelength of 808nm with power of 1 W modulated by optical chopper at 30Hz, was used. For spatial averaging the integrating sphere IS200-4, (Thorlabs) was applied. This light was measured by broadband (0.1-20 μm) UM9B-BL-DA pyroelectric photodetector(Gentec-EO). The modulated signal from the detector was recovered by lock-in amplifier SR 830 (Stanford Research). The signal coming out from the integrating sphere was attenuated with neutral density filter in order to set the light intensity to the optimum of dynamic range for detector and lock-in amplifier. The ratio between emitted and absorbed light gives an energy yield. This value than is transformed to the quantum yield taking into the account difference in photon energies for laser and PL band (for PL band was used average energy). The quantum yield value was corrected by transmission of applied edge-pass filters.

23

Supporting Information Available. Experimental details, additional TEM and HRTEM images. This material is available free of charge *via* the Internet at http://pubs.acs.org.

References.

[1] van Veggel, F. C. J. M. Near-Infrared Quantum Dots and Their Delicate Synthesis, Challenging Characterization, and Exciting Potential Applications. *Chem. Mater.* **2014**, *26*, 111−122.

[2] Kovalenko, M. V.; Schaller, R. D.; Jarzab, D.; Loi, M. A.; Talapin, D. V. Inorganically Functionalized PbS−CdS Colloidal Nanocrystals: Integration into Amorphous Chalcogenide Glass and Luminescent Properties. *J. Am. Chem.Soc.* **2012**, *134*, 2457−2460.

[3] Pietryga, J. M.; Werder, D. J.; Williams, D. J.; Casson, J. L.; Schaller, R. D.; Klimov, V. I.; Hollingsworth, J. A. Utilizing the Lability of Lead Selenide to Produce Heterostructured Nanocrystals with Bright, Stable Infrared Emission. *J. Am. Chem. Soc.* **2008**, *130*, 4879-4885.

[4] Zhao, H.; Chaker, M.; Wu, N.; Ma, D. Towards Controlled Synthesis and Better Understanding of Highly Luminescent PbS/CdS Core/Shell Quantum Dots *J. Mater. Chem.* **2011**, 21, 8898-8904.

[5] Friend, R. H.; Gymer, R. W.; Holmes, A. B.; Burroughes, J. H.; Marks, R. N.; Taliani, C.; Bradley, D. D. C.; Dos Santos, D. A.; Bredas, J. L.; Logdlund, M.; Salaneck, W. R. Electroluminescence in Conjugated Polymers. *Nature* **1999**, *397*, 121-128.

[6] Jasieniak, J.; Padicifico, J.; Signorini, R.; Chiasera, A.; Ferrari, M.; Martucci, A.; Mulvaney, P. Luminescence and Amplified Stimulated Emission in CdSe–ZnS-Nanocrystal-Doped TiO_2 and ZrO_2 Waveguides. *Adv. Funct. Mater.* **2007**, *17*, 1654.-1662

[7] Pang, L.; Shen, Y.; Tetz, K.; Fainman, Y. PMMA Quantum Dots Composites Fabricated via Use of Pre-polymerization. *Opt. Express.* **2005**, *13*, 44-49.

[8] Suárez, I.; Gordillo, H.; Abargues, R.; Albert, S.; Martínez-Pastor, J. Photoluminescence Waveguiding in CdSe and CdTe QDs-PMMA Nanocomposite Films. *Nanotechnology* **2011**, *22*, 435202-8.

[9] Chang, T.-W. F.; Maria, A.; Cyr, P. W.; Sukhovatkin, V.; Levina, L.; Sargent, E. H. High near-infrared photoluminescence quantum efficiency from PbS nanocrystals in polymer films. *Synthetic Metals*, **2005**, *148*, 257-261.

10 Wang, M.; Zhang, M.; Qian, J.; Zhao, F.; Shen, L.; Scholes, G.; Winnik, M. Enhancing the Photoluminescence of Polymer-Stabilized CdSe/CdS/ZnS Core/Shell/Shell and CdSe/ZnS Core/Shell Quantum Dots in Water through a Chemical-Activation Approach. *Langmuir* **2009**, *25*, 11732-11740.

11 Sundar, V. C.; Eisler, H. J.; Bawendi, M. G. Room-Temperature, Tunable Gain Media from Novel II–VI Nanocrystal–Titania Composite Matrices. *Adv. Mater*. **2002**, *14*, 739-743.

12 Petruska, M. A.; Malko, A. V.; Voyles, P. M.; Klimov, V. I. High-Performance, Quantum Dot Nanocomposites for Nonlinear Optical and Optical Gain Applications. *Adv. Mater*, **2003**, *15*, 610-613.

13 Liao, Y.; Xu, Y.; Chan, Y. Semiconductor Nanocrystals in Sol–gel Derived Matrices. *Phys.Chem.Chem.Phys*, **2013**, *15*, 13694-13704.

14 Tetsuka, H.; Ebina, T.; Mizukami, F. Highly Luminescent Flexible Quantum Dot–Clay Films. *Adv. Mater.* **2008**, *20*, 3039-3043.

15 Yoon, M.; Kim, Y.; Cho, J. Multifunctional Colloids with Optical, Magnetic, and Superhydrophobic Properties Derived from Nucleophilic Substitution-Induced Layer by-Layer Assembly in Organic Media. *ACS Nano* **2011**, *5*, 5417–5426.

16 Liu, B.; Ren, T.; Zhang, J. R.; Chen, H. Y.; Zhu, J. J.; Burda, C. Spectroelectrochemistry of Hollow Spherical CdSe Quantum Dot Assemblies in Water. *Electrochem. Commun.* **2007**, *9*, 551-557.

17 Kovalenko, M. V.; Scheele, M.; Talapin, D. V. Colloidal Nanocrystals with Molecular Metal Chalcogenide Surface Ligands. *Science* **2009**, *324*, 1417-1420.

18 Talapin, D. V.; Lee, J. S.; Kovalenko, M. V.; Shevchenko, E. V. Prospects of Nanocrystal Solids as Electronic and Optoelectronic Materials. *Chem. Rev.* **2010**, *110* , 389-458.

19 Humer, M.; Guider, R.; Jantsch, W.; Fromherz, T. Integration, Photostability and Spontaneous Emission Rate Enhancement of Colloidal PbS Nanocrystals for Si-based Photonics at Telecom Wavelengths. *Opt. express* **2013**, *21*, 18680-18688.

20 Novak, S.; Scarpantonio, L.; Novak, J.; Dai Pre, M.; Martucci, A.; Musgraves, J. D.; McClenaghan, N. D.; Richardson, K. Incorporation of Luminescent CdSe/ZnS Core-shell Quantum Dots and PbS Quantum Dots into Solution-derived Chalcogenide Glass Films. *Opt. Mater. Express* **2013**, *3*, 729-738.

25

[21] Kovalenko, M. V. Chemical Design of Nanocrystal Solids. *Chimia* **2013**, *67*, 316-321.

[22] Steckel, J.S.; Coe-Sullivan, S.; Bulović, V.; Bawendi, M. *Adv. Mater.* **2003**,*15*, 1862.

[23] Wehrenberg, B.L.; Wang, C.; Guyot-Sionnest, P. *J. Phys. Chem. B*, **2002**, *106*, 10634.

[24] Tsokkou, D.; Papagiorgis, P.; Protesescu, L.; Kovalenko, M.V.; Choulis, S.A.; Christofides, C.; Itskos, G.; Othonos. A. Photophysics of PbS Quantum Dot Films Capped with Arsenic Sulfide Ligands. *Advanced Energy Materials*. **2014**, 1301547.

[25] Lambright, S.; Butaeva, E. V.; Razgoniaeva, N.; Hopkins, T.; Smith, B.; Perera, D. N.; Corbin, J.; Khon, E.; Thomas, R.; Moroz, P.; Mereshchenko, A. S.; Tarnovsky, A. N.; Zamkov, M. Enhanced Lifetime of Excitons in Non-Epitaxial Au/CdS Core/Shell Nanocrystals. *ACS Nano* **2014**, *8*, 352-361.

[26] Zhitomirsky, D.; Voznyy, O.; Hoogland, S.; Sargent, E. H. Measuring Charge Carrier Diffusion in Coupled Colloidal Quantum Dot Solids. *ACS Nano*, **2013**, *7*, 5282–5290.

[27] Chandler, R. E.; Houtepen, A. J.; Nelson, J.; Vanmaekelbergh, D. Electron Transport in Quantum Dot Solids: Monte Carlo Simulations of the Effects of Shell Filling, Coulomb Repulsions, and Site Disorder. *Phys. Rev. B* **2007**, *75*, 085325-10.

[28] Fafarman, A. T.; Koh, W. K.; Diroll, B. T.; Kim, D. K.; Ko, D. K.; Oh, S. J.; Ye, X. C.; Doan-Nguyen, V.; Crump, M. R.; Reifsnyder, D. C.; Murray, C. B.; Kagan, C. R. Thiocyanate-Capped Nanocrystal Colloids: Vibrational Reporter of Surface Chemistry and Solution-Based Route to Enhanced Coupling in Nanocrystal Solids. *J. Am. Chem. Soc.* **2011**, 133, 15753– 15761.

[29] Lee, J. S.; Kovalenko, M. V.; Huang, J.; Chung, D. S.; Talapin, D. V. Band-like Transport, High Electron Mobility and High Photoconductivity in All-Inorganic Nanocrystal Arrays. *Nat. Nanotechnol.* **2011**, 6, 348– 352

[30] Liu, Y.; Tolentino, J.; Gibbs, M.; Ihly, R.; Perkins, C. L.; Liu, Y.; Crawford, N.; Hemminger, J. C.; Law, M. PbSe Quantum Dot Field-Effect Transistors with Air-Stable Electron Mobilities above 7 cm^2 V^{-1} s^{-1}. *Nano Lett.* **2013**, 13, 1578– 1587

[31] Tangirala, R.; Baker, J. L.; Alivisatos, A. P.; Milliron, D. J. Modular Inorganic Nanocomposites by Conversion of Nanocrystal Superlattices. *Angew. Chem., Int. Ed.* **2010**, 49, 2878– 2882

[32] Nag, A.; Chung, D. S.; Dolzhnikov, D. S.; Dimitrijevic, N. M.; Chattopadhyay, S.; Shibata, T.; Talapin, D. V. Effect of Metal Ions on Photoluminescence, Charge Transport, Magnetic and

26

Catalytic Properties of All-Inorganic Colloidal Nanocrystals and Nanocrystal Solids. *J. Am. Chem. Soc.* **2012**, 134, 13604-13615.

[33] Llordes, A.; Garcia, G.; Gazquez, J.; Milliron, D. J. Tunable Near-Infrared and Visible-Light Transmittance in Nanocrystal-in-Glass Composites. *Nature* **2013**, 500, 323-326.

[34] Khon, E.; Lambright, S.; Khon, D.; Smith, B.; O'Connor, T.; Moroz, P.; Imboden, M.; Diederich, G.; Perez-Bolivar, D.; Anzenbacher, P.; Zamkov, M. Inorganic Solids of CdSe Nanocrystals Exhibiting High Emission Quantum Yield. *Adv. Funct. Mater.* **2012**, *22*, 3714-3722.

[35] Diederich, G.; O'Connor, T.; Moroz, P.; Kinder, E.; Khon, E.; Perera, D.; Lorek, R.; Lambright, S.; Imboden, M.; Zamkov, M. Harvesting Solar Energy by Means of Charge-Separating Nanocrystals and Their Solids. *J. Vis. Exp.* **2012**, *66*, e4296.

[36] Pathan, H. M.; Lokhande, C. D. Deposition of Metal Chalcogenide Thin Films by Successive Ionic Layer Adsorption and Reaction (SILAR) Method. *Bull. Mater. Sci.* **2004**, *27*, 85-111.

[37] Manna, L.; Scher, E. C.; Li, L.-S.; Alivisatos, A. P. Epitaxial Growth and Photochemical Annealing of Graded CdS/ZnS Shells on Colloidal CdSe Nanorods. *J. Am. Chem. Soc.* **2002**, *124*, 7136– 7145.

[38] Carbone, L.; Cozolli, P. D. Colloidal Heterostructured Nanocrystals: Synthesis and Growth Mechanisms. *Nano Today,* **2010,** *5*, 449-493.

[39] Donega, C. D. Synthesis and Properties of Colloidal Heteronanocrystals. *Chem. Soc. Rev.* **2011**, 40, 1512– 1546.

[40] Moroz, P.; Kholmicheva, N.; Mellott, B.; Liyanage, G.; Rijal, U.; Bastola, E.; Huband, K.; Khon, E.; McBride, K.; Zamkov, M. Suppressed Carrier Scattering in CdS-Encapsulated PbS Nanocrystal Films. *ACS Nano* **2013**, *7*, 6964-6977.

[41] Helms, V. Fluorescence Resonance Energy Transfer". Principles of Computational Cell Biology. Weinheim: Wiley-VCH. p. 202. **2008**

[42] Hines, M. A.; Scholes, G. D. Colloidal PbS Nanocrystals with Size-Tunable Near-Infrared Emission: Observation of Post-Synthesis Self-Narrowing of the Particle Size Distribution. *Adv. Mater.* **2003**, *15*, 1844–1849.

[43] Yu, W. W.; Peng, X. Formation of High-Quality CdS and Other II - VI Semiconductor Nanocrystals in Noncoordinating Solvents: Tunable Reactivity of Monomers. *Angew. Chem.* **2002**, *114*, 2474-2477.

27

44 Kinder, E.; Moroz, P.; Diederich, G.; Johnson, A.; Kirsanova, M.; Nemchinov, A.; O'Connor, T.; Roth, D.; Zamkov, M. Fabrication of All-Inorganic Nanocrystal Solids through Matrix Encapsulation of Nanocrystal Arrays. *J. Am. Chem. Soc.* **2011**, *133*, 20488-20499

45 Semonin, O. E.; Johnson, J. C.; Luther, J. M.; Midgett, A. G.; Nozik, A. J.; Beard, M. C. Absolute Photoluminescence Quantum Yields of IR-26 Dye, PbS, and PbSe Quantum Dots *J. Phys. Chem. Lett.* **2010,** *1,* 2445-2450.